JOURNAL OF CASTING
& MATERIALS ENGINEERING

AGH UNIVERSITY OF SCIENCE AND TECHNOLOGY
FACULTY OF FOUNDRY ENGINEERING

JCME

Contents

Identification of Gas Products from Pyrolysis Process of Waxes Used in Lost-Wax Casting Technology

Sylwia Żymankowska-Kumon[a]*, Joanna Kolczyk-Tylka[b]

[a] AGH University of Science and Technology, Faculty of Foundry Engineering, Department of Foundry Processes Engineering, Reymonta 23, 30-059 Krakow, Poland
[b] AGH University of Science and Technology, Faculty of Foundry Engineering, Department of Molding Materials, Mold Technology and Cast Non-Ferrous Metals, Reymonta 23, 30-059 Krakow, Poland
e-mail: szk@agh.edu.pl

Abstract

Foundry waxes currently used in lost-wax casting technology are composed of paraffin, stearin, and – to a lesser extent – ceresin, polyethylene wax, and other natural and synthetic waxes. Most of these compounds are non-toxic; however, they may release aromatic hydrocarbons as a result of exposure to high temperatures. Based on a chromatographic analysis (pyrolysis gas chromatography-mass spectrometry, Py-GC/MS), the compounds that are separated from the popular wax mixtures used in foundries were evaluated (as well as the impact they may have on foundry workers). For this purpose, the three main stages of the process (wax, burnout, and pouring) were analyzed, and the appropriate test temperature was chosen (similar to the actual conditions during the process).

1. INTRODUCTION

Lost-wax casting is the process by which a duplicate metal sculpture (like silver, gold, brass, or bronze) is cast from an original sculpture. The steps used in casting small bronze sculptures are fairly standardized, though the process varies between foundries today. In modern industrial use, the process is called investment casting [1, 2]. Variations of the process include "lost mold," which recognizes that materials other than waxes can be used (such as tallow, resin, tar, and textile), and "waste wax process" or "waste mold casting," because the mold is destroyed to remove the cast item [3–5].

There is a very thin line between investment casting and lost-wax casting. We can differentiate the processes; if the investment casting is done by a wax pattern mold, then it is called lost-wax casting. In lost-wax casting, the wax patterns are manually prepared for each piece [3, 4], while in investment casting, metals are formed to produce high-quality casting components:

- Lost-wax casting is mainly used for small parts such as jewelry casting or even fashion accessories, while investment casting is highly used for the manufacture of complex or critical parts.
- In lost-wax casting, only one pattern can be used to make numerous patterns (even though the pattern is lost or melted), while through investment casting, one can produce an exact replica of the desired casting.

- In lost-wax casting, the manufacturer focuses on precise wax or mold design, while in investment casting, they focus on metals like nickel alloys, copper alloys, cobalt-based alloys, or super alloys [3].

Casts can be made of the wax model itself (the direct method) or of a wax copy of a model that need not be made of wax (the indirect method). Figure 1 shows the following steps for the indirect process [5–7].

Fig. 1. Scheme of all steps in lost-wax casting technology

From these steps, the most important ecological steps are the wax, burnout, and pouring phases. The exposure to temperature is different.

In the "wax" step, molten wax is poured into a matrix-mold (made of the original model or sculpture from latex, polyurethane rubber, or silicone, for example). The substances that are used in lost-wax casting technology can be divided into three main groups: waxes, fatty acids, and wax substances.

Waxes are esters of higher fatty acid monocarboxylic and higher monohydric alcohols of even numbers of carbon atoms (from C_{16} to C_{36}). The model mixtures are not homogeneous [4, 7, 8]; these are mixtures with various chemical compositions, but they have one common feature – they consist of linearly placed particles containing between 20 to 70 CH groups. Taking into account the wax components in model mixtures, these particles very often contain ketone, oxide, and alcoholic substances together with the esters of higher fatty acids [9–11]. The temperature range of liquid wax is between 100-150°C (depending on the type of wax used).

The "burnout step" is intended to get rid of about 80% of the wax from the ceramic shell. The temperature range of this process is about 95–110°C. The last "pouring step" is related to cleaning the ceramic shell and removing all traces of moisture and the rest of the wax model. The temperature range of this process is between 870–1040°C.

All of these steps generate a lot of odors and chemical substances (mainly from the wax model), so the main purpose of this research is to analyze the types of these compounds by the pyrolysis gas chromatography-mass spectrometry method (Py-GC/MS).

2. MATERIALS AND RESEARCH METHODOLOGY

Two types of wax mixtures used in lost-wax casting technology were selected for the study. All of the basic parameters of the samples are presented in Table 1. The "W1" sample (not a popular wax mixture in foundries) generates many odors and has a smaller kinematic viscosity (dynamic). The solidification point of "W1" is lower than the "W2" sample (which is the most popular lost-wax casting technology). However, the "W1" wax mixture is about 12% cheaper, and it is characterized by better shape reproduction in the case of thick-walled and massive simple castings (a slight shrinkage of the wax when pouring it into the mold).

At a temperature of 150°C, the samples were pyrolyzed in a tube furnace in an inert atmosphere (argon). The emitted compounds were adsorbed on active carbon; after this process, they were extracted by means of diethyl ether. At a temperature of 1000°C, the samples were mainly analyzed by the pyrolysis gas chromatography (Py-GC/MS) method, which is based on transforming a solid sample (2–5 mg) into gas by heating it in an atmosphere of inert gas (helium) in a "Py" Pyroprobe 5000 pyrolyzer (CDS Analytical Inc.), which is accompanied by thermal decomposition. It has a platinum ribbon or coil, which enables the heating of a sample to any temperature within a range of 250–1100°C [12].

The obtained mixture of compounds is separated on a chromatographic column (Restek Rxi-5Sil fused silica) in a "GC" chromatograph (Focus GC, Thermo Scientific). A temperature program was applied: an initial temperature

of 40°C was held for 5 min; ramped up by 5°C/min up to 150°C and held for 5 min; then, up to 250°C with a heating rate of 10°C/min and maintained for 5 min (helium carrier gas at 1 ml/min; sample split ratio – 1:20). The separated compounds are analyzed in an "MS" mass spectrometer (ISQ Thermo Scientific) in the full-range mass number/ charge number (*m/z*). Electron ionization (70 eV) at a temperature of 250°C was then applied [12–14].

3. RESULTS

The compounds found after the pyrolytic decomposition of the samples of the wax mixtures are summarized in Table 2. A comparison of the measured mass spectra to the National Institute of Standards Technology database (NIST MS Search 2.0) and its own patterns (e.g., aromatic hydrocarbons like benzene, toluene, etc.) gave the possible types for the released compounds.

As a result of a temperature of 150°C (Fig. 2), only about 30% of the compounds were identified in the pyrolytic products as compared to the tests at 1000°C. Both samples contained similar compounds with a predominance for the W1 sample, which additionally have fatty acids (myristic acid, lignoceric acid, and isopropyl myristate – the ester of isopropyl alcohol and myristic acid for Sample W2). Both samples mainly contained fatty acids and some organic compounds based on the benzene ring and α-pinene of the terpene class (Tab. 2), which are the primary constituents of turpentine (a solvent for waxes).

At 1000°C, the chromatographic spectrum (Fig. 3) is much more complex and contains many different compounds, with a predominance for the W1 sample (mainly simple hydrocarbons). In the gaseous products for retention times within a range of 1 to 24 minutes, Sample W1 recorded many intense peaks coming from low molecular weight hydrocarbons. These compounds can be divided into the following groups: aromatic hydrocarbons with a benzene ring, carboxylic acids (e.g., acetic and butyric acid – wax solvents), ketones (e.g., diacetyl – simple ketones are, in general, not highly toxic), and alcohols (also wax solvents). Typical compounds of wax mixtures are glycerol (another name – glycerin) and azulene. Chloroform was probably also used as a solvent. For retention times within the range of 24 to 50 minutes, many intense peaks coming from high molecular weight hydrocarbons were recorded, mainly fatty acids (similar to 150°C). As compared to W2, wax mixture W1 generates about 40% more compounds, which is its disadvantage.

According to the steps of the lost-wax casting technology, more dangerous for human health is the "pouring step", where the temperature of the process is about 1000°C. An accumulation of toxic compounds occurs within this range.

Table 1
Properties of wax mixtures

Sample/Parameters	Solidification point, °C	Dropping point, °C	Kinematic viscosity at 100°C, mm²/s	Penetration at 25°C	Acid number, mg KOH/g
W1	79.25	83.14	8.43	11	57.25
W2	84.34	87.12	9.95	12	48.38

Table 2
Results of Py-GC/MS investigations for selected temperature points

Peak No.	Name of compound	No. CAS	Molecular weight, u	Retention time R_T, min			
				W1		W2	
				150°C	1000°C	150°C	1000°C
1	Carbon dioxide	124–38–9	44	–	4.57	–	–
2	Acetic acid	64–19–7	60	–	8.12	–	–
3	Propan-2-ol	67–63–0	60	–	10.12	–	–
4	Cyclobutanone	1191–95–3	70	–	13.12	–	–
5	Methyl acetate	79–20–9	74	–	14.01	–	–
6	Benzene	71–43–2	78	–	14.39	–	14.37
7	Diacetyl	431–03–8	86	–	15.24	–	–
8	Butyric acid	107–92–6	88	–	18.12	–	–
9	Pentan-1-ol	71–41–0	88	–	18.24	–	–
10	Toluene	108–88–3	92	–	19.01	–	–
11	Glycerol	56–81–5	92	–	19.48	–	19.50
12	Phenylethyne	536–74–3	102	–	20.01	–	–
13	Styrene	100–42–5	104	–	21.12	–	–
14	Ethylbenzene	100–41–4	106	–	22.04	–	–
15	Indene	95–13–6	116	–	22.58	–	–
16	Chloroform	67–66–3	119	–	23.24	–	–
17	Azulene	275–51–4	128	–	23.48	–	24.01
18	Naphthalene	91–20–3	128	–	24.12	–	–
19	Benzo[c]thiophene	270–82–6	134	25.12	25.28	25.11	25.30
20	α-pinene	80–56–8	136	27.35	27.48	27.29	27.51
21	Caprylic acid	124–07–2	144	29.35	29.48	29.40	29.54
22	Acenaphthylene	208–96–8	152	31.33	32.08	31.29	32.10
23	Benzophenone	119–61–9	182	33.57	34.12	34.01	34.15
24	Bibenzyl	103–29–7	182	35.48	36.01	35.51	36.02
25	Lauric acid	143–07–7	200	37.01	37.25	37.03	37.31
26	Myristic acid	544–63–8	228	–	39.48	38.57	39.54
27	Hexadecan-1-ol	36653–82–4	242	–	41.34	–	41.28
28	Palmitic acid	57–10–3	256	–	42.59	–	43.01
29	Isopropyl myristate	110–27–0	270	45.01	44.58	–	44.52
30	Stearic acid	57–11–4	284	–	46.12	–	46.15
31	Lignoceric acid	557–59–5	368	48.03	47.48	–	47.54
32	1-Triacontanol	593–50–0	438	–	49.37	–	49.41
33	Biphenyl	92–52–4	154	–	53.48	–	53.50
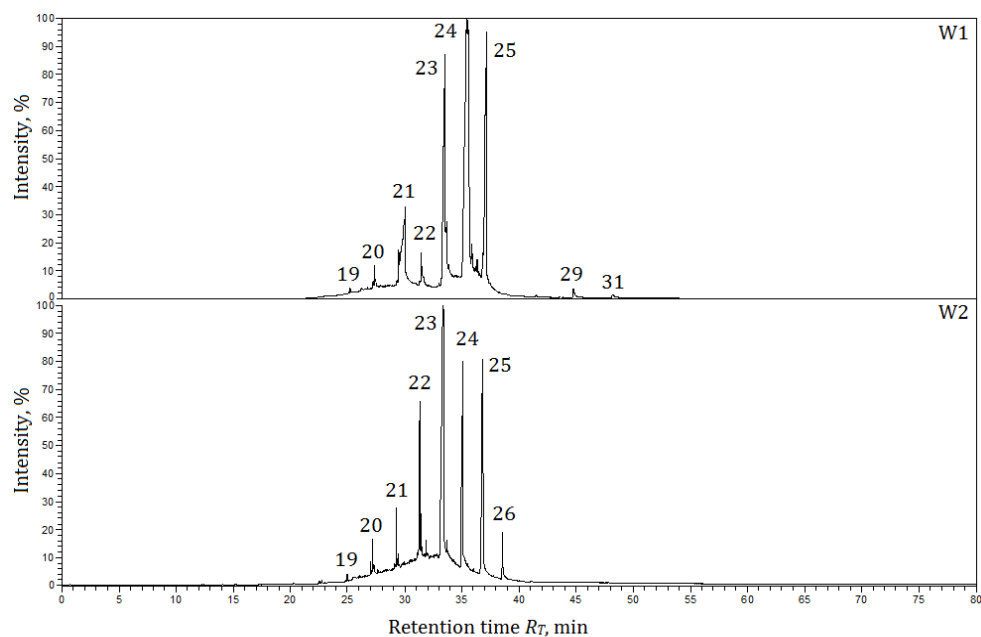
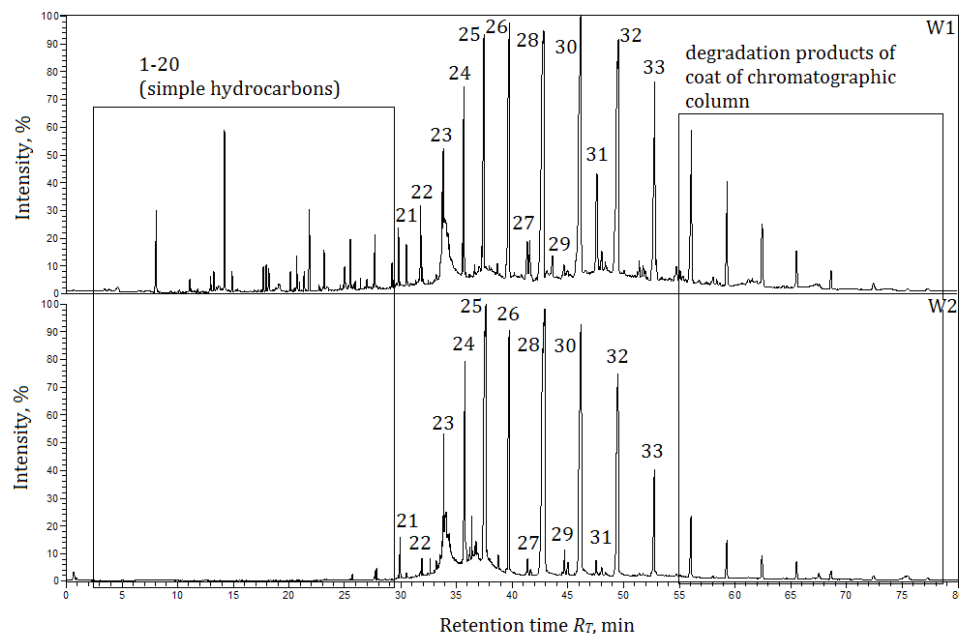**Fig. 2.** Chromatograms for samples at 150°C

Fig. 3. Chromatograms for samples at 1000°C

4. CONCLUSIONS

The wax mixtures are all chemicals that can affect human health. The gases that the waxes produce during burnout and pouring are dangerous. Heat (definitely a part of the casting process) causes chemical reactions to accelerate (and sometimes starts them). Specific chemicals include wax and plastic fumes from the burnout. When waxes burn, they release many toxic and irritating compounds (including aromatic hydrocarbons). Burning the organic chemicals added to wax such as rosin, glycerin, petroleum jelly, azulene, fatty acid, etc. will release carbon monoxide and other toxic decomposition products.

In connection with the research and taking into account the parameters of the wax mixtures, the use of wax mixture W2 would be more beneficial for safety reasons. It generates fewer toxic gases, mainly due to the aromatic hydrocarbons. During the burnout and pouring steps, it is recommended to use exhaust gas installations with filters that can absorb the gases.

Acknowledgements

REFERENCES

[1] Haratym R., Biernacki R. & Myszka D. (2008). *Ekologiczne wytwarzanie dokładnych odlewów w formach ceramicznych*. Warszawa: Oficyna Wydawnicza Politechniki Warszawskiej.

[2] Allendorf H. (1960). *Odlewanie precyzyjne za pomocą modeli wytapianych*. Warszawa: Państwowe Wydawnictwa Techniczne.

[3] Energy Technocast Pvt. Ltd. (2015). Promo materials (leaflet).

[4] Zych J., Kolczyk J. & Snopkiewicz T. (2013). New investigation method of the permeability of ceramic moulds applied in the investment casting technology. *Archives of Foundry Engineering*, 13(2), 107–112.

[5] Lewandowski J.L. (1995). *Tworzywa na formy odlewnicze*. Kraków: Akapit.

[6] Baron J., Miazga B., Ntaflos T., Puziewicz J. & Szumny A. (2016). Beeswax remnants, phase and major element chemical composition of the bronze age mould from Gaj Oławski (SW Poland). *Archaeological and Anthropological Sciences*, 8(1), 187–196. Doi: 10.1007/s12520-014-0225-0.

[7] Freitas C.A., Vieira Í.G., Sousa P.H., Muniz C.R., Gonzaga M.L. & Guedes M.I. (2016). Carnauba wax p-methoxycinnamic diesters: Characterisation, antioxidant activity and simulated gastrointestinal digestion followed by in vitro bioaccessibility. *Food Chemistry*, 196, 1293–1300. Doi: 10.1016/j.foodchem.2015.10.101.

[8] Bonaduce I., Cito M. & Colombini M.P. (2009). The development of a gas chromatographic-mass spectrometric analytical procedure for the determination of lipids, proteins and resins in the same paint micro-sample avoiding interferences from inorganic media. *Journal of Chromatography A*, 1216, 5931–5939. Doi: 10.1016/j.chroma.2009.06.033.

[9] Chica E., Agudelo S. & Sierra N. (2013). Lost wax casting process of the runner of a propeller turbine for small hydroelectric power plants. *Renewable Energy*, 60, 739–745. Doi: 10.1016/j.renene.2013.06.030.

[10] Bombelli P., Howe C.J. & Bertocchini F. (2017). Polyethylene bio-degradation by caterpillars of the wax moth Galleria mellonella. *Current Biology,* 27(8), R292–R293. Doi: 10.1016/j.cub.2017.02.060.

[11] Regert M., Langlois J. & Colinart S. (2005). Characterisation of wax works of art by gas chromatographic procedures. *Journal of Chromatography A*, 1091, 124–136. Doi: 10.1016/j.chroma.2005.07.039.

[12] Grabowska B., Kaczmarska K., Bobrowski A., Żymankowska-Kumon S. & Kurleto-Kozioł Ż. (2017). TG-DTG-DSC, FTIR, DRIFT, and Py-GC-MS Studies of Thermal Decomposition for Poly(sodium acrylate)/Dextrin (PAANa/D) – New Binder Bio-Co3. *Journal of Casting & Materials Engineering*, 1(1), 27–32. Doi: 10.7494/jcme.2017.1.1.27.

[13] Russo M.V. & Avino P. (2012). Characterization and Identification of Natural Terpenic Resins employed in "Madonna con Bambino e Angeli" by Antonello da Messina using Gas Chromatography-Mass Spectrometry. *Chemistry Central Journal*, 6(1), 59–69. Doi: 10.1186/1752-153X-6-59.

[14] Żymankowska-Kumon S. (2016). Ecological assessment of foundry binders from cold-box technology by gas chromatography method. *World Scientific News,* 57, 554–561.

Influence of Fluoride Ions in Artificial Saliva Solution to Corrosion Behavior of Ti-6Al-4V and Ti-10Mo-4Zr Titanium Alloys

Joanna Loch[a]*, Halina Krawiec[a]

[a]AGH University of Science and Technology, Faculty of Foundry Engineering, Reymonta 23, 30-059 Krakow, Poland
*e-mail: loch@agh.edu.pl

Abstract

Titanium alloys used in medical applications (especially dentistry) are exposed to the actions of various compounds that appear periodically in the mouth. Fluorine compounds are dangerous for the surface of titanium alloys, because they generate a dissolution of the passive layer. In this way, they destroy the surface of dental implants and cause the absorption of metal ions into the human body.
The presented work was aimed to describe the effect of fluoride ions on the corrosive behavior of the commercial Ti-6Al-4V and new Ti-10Mo-4Zr alloys that can be used in stomatology. Electrochemical measurements such as open circuit potential (OCP), linear sweet voltamperometry (LSV) and impedance spectroscopy (EIS) were performed to get information on the corrosive behavior of titanium in artificial saliva solutions (MAS) with different concentrations of NaF. It has been revealed that a high concentration of fluoride ions enhance the current density in the anodic domain, especially for the Ti-10Mo-4Zr alloy. EIS measurements performed at a potential of 0.5 V vs. AgCl (3 M KCl) show that the Ti-10Mo-4Zr alloy has a typical two-layer structure of its passive film. This passive film consists of the outer and inner layers, respectively. The resistance of the outer layer is significantly lower than the resistance of the inner layer.

Keywords:

titanium alloys, artificial saliva solution, fluoride ions, corrosion

1. INTRODUCTION

In recent years, research on titanium alloys in medical applications has become very popular. The research direction is focused on the search for new titanium alloys and determining their physicochemical properties. In orthopedics and dentistry, a very important aspect is the durability and functionality of endoprostheses. Titanium alloys are used for biomedical applications because they have suitable mechanical properties (as endoprothesis), good biocompatibility with tissues, and very good resistance to local corrosion. Currently, Ti-6Al-4V is a commonly used titanium alloy. Only after extended use of this titanium alloy did we realize that aluminum and vanadium can have adverse effects on the human body. Therefore, new titanium alloys have non-toxic elements [1–3]. Research on the corrosion resistance of the new titanium alloys is designed to isolate those alloys that will have similar corrosion resistance as do alloys with aluminum and vanadium. There are many publications describing alloys with the additions of niobium, tantalum, zirconium, and molybdenum under various conditions [4–14].

The determination of the influence of an electrolyte (which is a simulated physiological solution) is important in the corrosion tests. In vivo tests, salt solutions are often used: Ringer and Hank's solution, artificial saliva solutions, and phosphorate buffered saline (PBS) with various organic and inorganic chemicals. Saliva solution composition is variable throughout the day, which results from the variety of products consumed. There are also substances that occur periodically; e.g., citric acid, calcium carbonate, and others. The content of fluoride (which also acidifies the environment) is characteristic for the composition of artificial saliva. Fluoride is located in the mouth because it is a component of toothpaste and mouthwash. In the case of people with titanium implants, this is dangerous [4, 15–18]. The too-long and frequent use of products containing F^- fluoride ions may dissolve the passive layer of alloys by the presence of hydrofluoric acid and its derivative compounds [19–24].

In this paper, the influence of fluoride ions on the corrosive behavior of both titanium alloys (Ti-6Al-4V and Ti-10Mo-4Zr) in a Mayer artificial saliva solution (MAS) is presented.

2. EXPERIMENTAL

2.1. Samples and solution

The Ti-6Al-4V commercial alloy and new biomedical Ti-10Mo-4Zr titanium alloy (Goodfellow) were used in this investigation. The titanium alloys were mechanically ground using abrasive papers (SiC) down to 4000 grit and polished using diamond pastes (3 and 1 μm). Finally the samples were polished using a 0.02 μm non-crystallizing colloidal silica suspension. Between each step, the specimens were ultrasonically cleaned in ethanol. In order to reveal the microstructure, both Ti alloy specimens were etched in a Koll's solution (5 ml HNO_3, 10 ml HF, 85 ml H_2O) for 5 seconds and rinsed in distilled water and then in ethanol.

The electrochemical tests were performed in a Mayer artificial saliva solution (MAS). The chemical composition of the MAS is presented in Table 1. Experimental measurements were performed by adding sodium fluoride in the following different amounts to the MAS solution (Tab. 2).

Table 1
Chemical compound of Mayer artificial saliva solution (MAS) in H_2O; pH = 6.4

Chemical compound, $g/l_{solution}$						
NaCl	KCl	$NaHCO_3$	Na_2HPO_4	KSCN	$Na_2S \cdot 9H_2O$	Urea
0.7	1.2	1.5	0.26	0.3	0.005	1.0

Table 2
Artificial saliva solution (MAS) with added sodium fluoride

Indication of solution	Content of NaF, $g/l_{solution}$	pH of solution
MAS + 5 NaF	5.0 g (~0.5%)	6.2
MAS + 25 NaF	25.0 g (~2.5%)	7.4

2.2. Experimental methodology

Global electrochemical experiments were carried out at 37°C using a PGSTAT302 AUTOLAB potentiostat/galvanostat with an FRA (frequency response analyzer) module. The corrosion tests were performed in a classical electrochemical cell where the following electrodes were placed: a platinum grid was used as a counter electrode, the specimen of the Ti alloy was a working electrode, and Ag/AgCl (a 3 M KCl solution) was a reference electrode. All measurements were made in MAS containing 5 and 25 g/l NaF, respectively.

The evolution of the open circuit potential (OCP) was measured for 24 h in the MAS solution at 37°C. The potentiodynamic polarization (LSV) curves were recorded for both Ti alloys in the MAS solution within a potential range of −1.0 to +2.5 V (vs. Ag/AgCl). The LSV curves were performed at a potential scan rate of 1 mV/s. Electrochemical impedance spectroscopy (EIS) diagrams were plotted within a frequency range of 100 kHz to a few mHz (30 points) using a 20 mV peak-to-peak sinusoidal potential difference. The experiments were performed after 1800 s of immersion at various applied potentials: in the anodic domain (0.5 V vs. Ag/AgCl). The impedance spectra were fitted by means of an equivalent circuit using the Z-view software package.

3. RESULTS AND DISCUSSION

3.1. Microstructure of titanium alloys

Commercial titanium alloy Ti-6Al-4V is composed of two metallic phases (the α– and β–phases). The average grain size are around 5–10 μm in both phases. By contrast, the second alloy (Ti-10Mo-4Zr) is composed of one β metallic phase. The grain size are roughly ten times larger than in the previous case – about 100 μm (Fig. 1). A detailed description of the chemical composition of the phases is presented in [9].
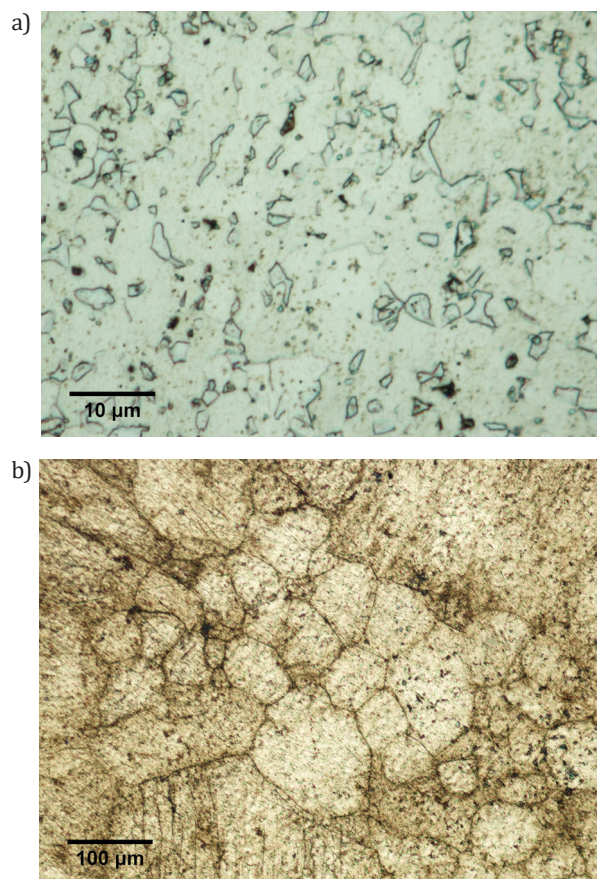

Fig. 1. Microstructure of titanium alloy: a) Ti-6Al-4V; b) Ti-10Mo-4Zr. Etching in Kroll's solution (HF-HNO_3-H_2O)

3.2. Open-circuit potential

The electrochemical tests confirmed that a high concentration of fluoride ions in a MAS promotes a significant deterioration of the passive layer formed at the surface of the Ti alloys.

Figure 2 shows that the open-circuit potential measured for both Ti alloys in a MAS is much lower in a solution containing fluoride ions. Moreover, the OCP values decrease when the concentration of NaF increases in an MAS. The open-circuit potential measured for both Ti alloys quickly attains a stable value in the MAS solution (Fig. 2). The potential values obtained after about 80,000 s (22 h) are around −7 mV for Ti-6Al-4V (Fig. 2a – dotted black line) and about −37 mV for Ti-10Mo-4Zr vs. Ag/AgCl (Fig. 2b – dotted black line), respectively. However, the value of the OCP measured for both Ti alloys in the MAS with NaF always obtained lower values than in an MAS. The potential values at the beginning of the measurement for the Ti-6Al-4V alloy assume lower values (from −800 to −590 mV vs. Ag/AgCl) as compared to the Ti-10Mo-4Zr alloy (from −500 to −300 mV vs. Ag/AgCl) and slightly increase over time. For the Ti-10Mo-4Zr alloy, the values of potential decrease, reaching a potential value of around −390 to −520 mV vs. Ag/AgCl (which is similar for both NaF contents).
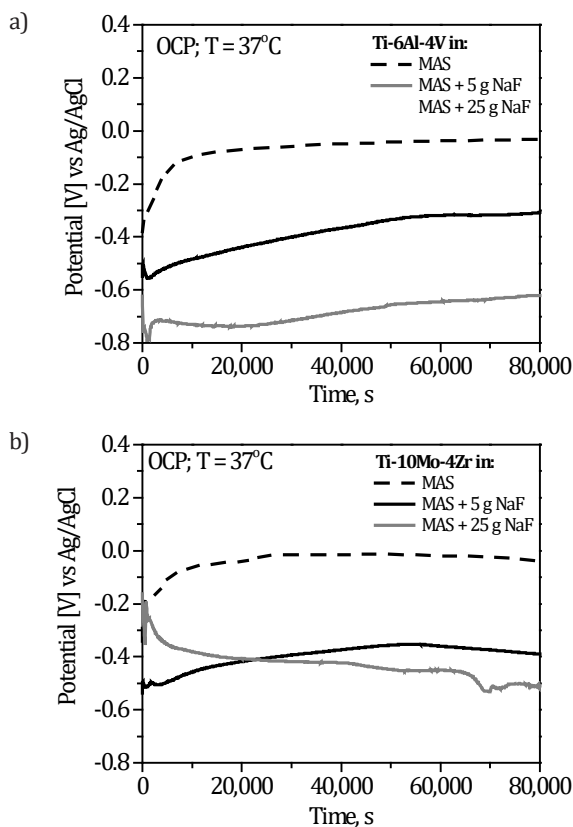
Fig. 2. Open-circuit potential of (a) Ti-6Al-4V and (b) Ti-10Mo-4Zr alloys in artificial saliva solution (MAS) and MAS with NaF

3.3. Linear sweep voltamperometry

In the next stage, linear sweep voltamperometry measurements were performed for the Ti-6Al-4V and Ti-10Mo-4Zr alloys in MAS and MAS-NaF solutions. The polarization curves obtained for both Ti alloys are presented in (Fig. 3). The current density in the anodic branch measured for both Ti alloys is significantly higher in the MAS solution containing sodium fluoride. Significant increases of the current

density in the anodic branch is observed for the Ti-10Mo-4Zr alloy in the MAS solution containing 25 g NaF (Fig. 3b).

Such a large difference in the current density registered in the anodic branch was not observed for the Ti-6Al-4V alloy in the MAS and MAS containing different concentrations of NaF. The LSV curves revealed that the current density in the anodic domain depends on the type of alloy and concentration of the fluoride ions. In Table 3, the current density values measured for both Ti alloys at an anodic potential of 0.5 V vs. Ag/AgCl are presented. Generally, the mono-phase Ti-10Mo-4Zr alloy exhibits a more active behavior in the anodic domain than the Ti-6Al-4V. Moreover, it can be noticed that a higher concentration of NaF in the MAS solution affects the value of the equilibrium potential for both Ti alloys. A higher concentration of NaF in the MAS solution shifts the equilibrium potential to a more negative potential (Fig. 3).
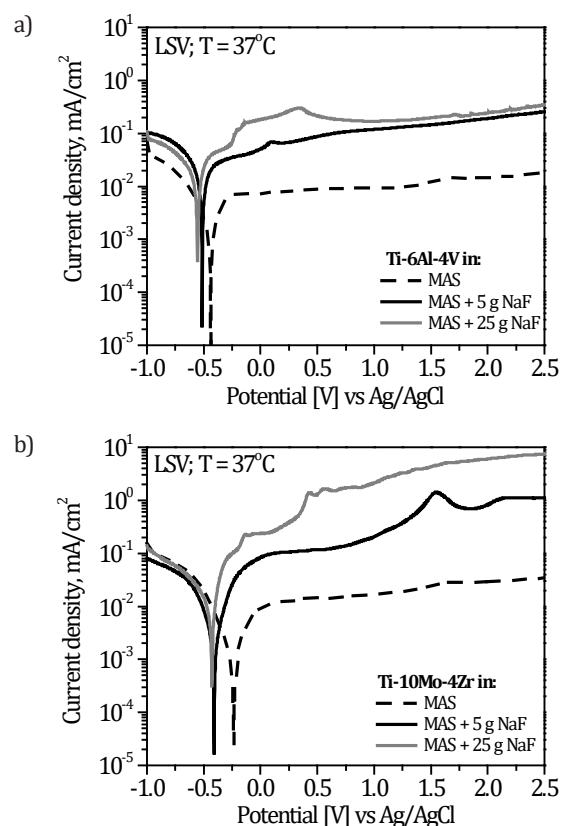

Fig. 3. Linear sweep voltamperometry of (a) Ti-6Al-4V and (b) Ti-10Mo-4Zr alloys in artificial saliva solution (MAS) and MAS with NaF

Table 3
Anodic current density values measured for Ti-6Al-4V and Ti-10Mo-4Zr alloys, respectively, at 0.5 V vs. Ag/AgCl in MAS and MAS with NaF solutions

Alloy /Solution	Current density, mA/cm²		
	MAS	**MAS + 5 g NaF**	**MAS + 25 g NaF**
Ti-6Al-4V	$8.8 \cdot 10^{-3}$	$85.5 \cdot 10^{-3}$	$202.3 \cdot 10^{-3}$
Ti-10Mo-4Zr	$8.0 \cdot 10^{-3}$	$114.9 \cdot 10^{-3}$	$986.5 \cdot 10^{-3}$

According to the literature data, the deterioration of the corrosive properties in the case of titanium and its alloys immersed in a solution of artificial saliva with the addition of fluorides largely corresponds to the Ti-F complex formed on the surface of the alloys in the form of compounds Na_2TiF_6, $TiOF_2$, TiF_4, and TiF_3 [24, 25]. Despite the low solubility of NaF in water, a reaction occurs (Eqs. (1) and (2)). The rate of the reaction taking place is not known; however, the resulting ions accelerate the dissolution of the passive layer of the alloys. If the solution is acidic (in our work, the MAS had a pH level of 6.4), the reaction mechanisms on the surface of titanium alloys can look like those of a solution of hydrofluoric acid HF [26]. The processes occurring on the surface of the titanium alloys in the presence of F^- ions are also present in the following reactions with hydrofluoric acid (Eqs. (3)–(5)), which is mainly attributed to the destruction of the surface [24, 27, 28]:

$$NaF + H_2O = Na^+ + OH^- + HF \tag{1}$$

$$2HF = H_2F^+ + F^- \tag{2}$$

$$TiO_2 + 2HF = TiOF_2 + H_2O \tag{3}$$

$$TiO_2 + 4HF = TiF_4 + 2H_2O \tag{4}$$

$$Ti_2O_3 + 6HF = 2TiF_3 + 3H_2O \tag{5}$$
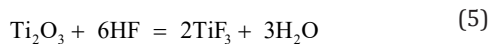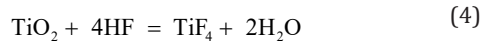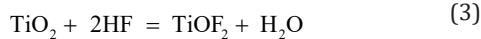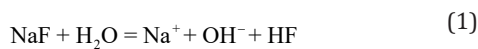
Figure 4 presents the behavior of titanium in solutions with the addition of NaF at various pH levels. When we deal with a solution with a slightly acidic pH, the passive layer is slowly dissolved (which is schematically indicated in Figure 4a). This is explained by the low OCP values and high anodic currents in the MAS solution with the addition of NaF. When the solution has a neutral pH, the presence of fluoride ions has no significant effect on the dissolution of the passive layer [29].
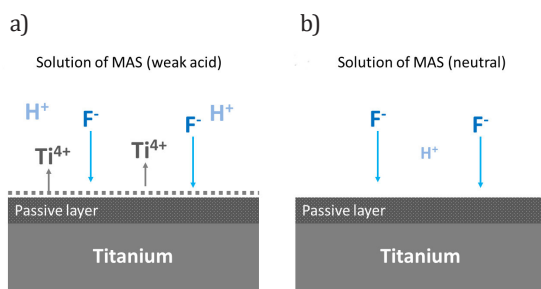

Fig. 4. Scheme of influence of F^- ions on surface layer of titanium and its alloys depending on pH level of solution: (a) solution with slightly acidic pH MAS and (b) neutral solution of MAS [26]

The effect on the instability of the passive layer of titanium alloys in contact with F^- ions depends on the chemical composition of the passive film. Fluoride is highly reactive for titanium alloy with molybdenum [30]. The increasing intensity of the dissolution of the Ti-10Mo-4Zr alloy at a potential of > 0.5 V vs. Ag/AgCl (Fig. 3b) is determined by the formation of fluoride compounds with molybdenum

on the surface. Primary molybdenum compounds MoF_6 and MoO_3 oxidize to form $MoOF_4$, which has much less resistance to corrosion [31]. Continuous exposure to fluorine reduces the protective properties of the passive layer, which corresponds to the reduced stationary potential.

The Ti-6Al-4V alloy contains vanadium; its passive layer is in the form of vanadium (III) oxide. In contact with hydrofluoric acid, it forms vanadium (III) fluoride according to Reaction (6):

$$V_2O_3 + 6HF \rightarrow 2VF_3 + 3H_2O \tag{6}$$
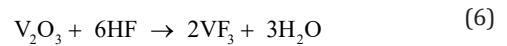
3.4. Electrochemical behavior in anodic domain

To confirm the obtained results and characterize the structures of the surface layers of the titanium alloys, an EIS measurement was carried out (Fig. 5) for each titanium alloy at a potential of 0.5 V vs. Ag/AgCl in MAS with the addition of sodium fluoride after previous chronoamperometry at a potential of 0.5 V vs. Ag/AgCl for 1200 s.
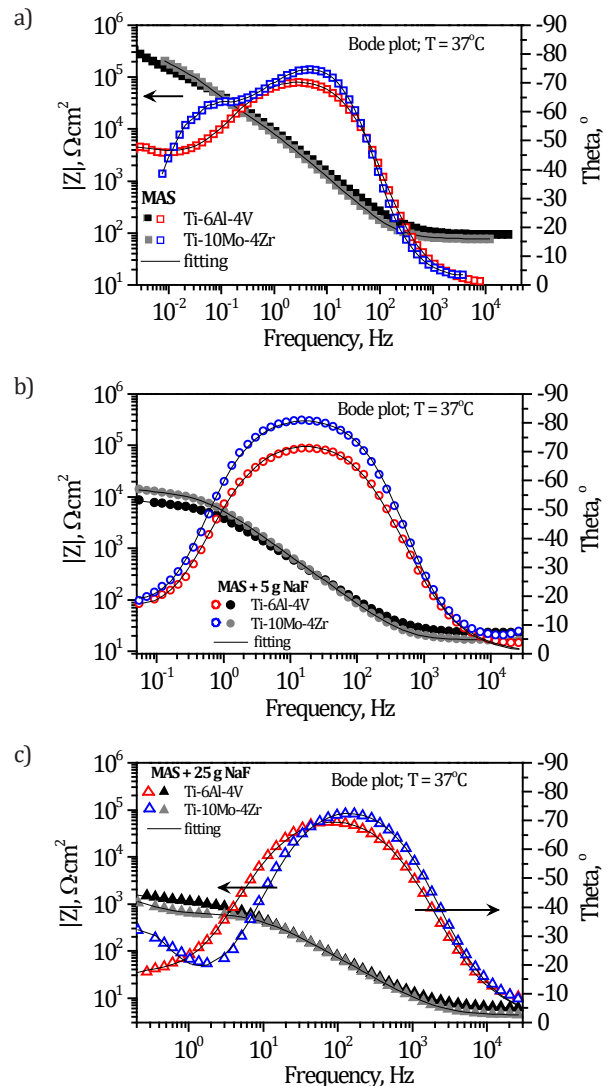

Fig. 5. Electrochemical impedance diagrams: Bode plots obtained on Ti-6Al-4V and Ti-10Mo-4Zr alloys in (a) MAS, (b) MAS + 5 g NaF, and (c) MAS + 25 g NaF at 37°C at 0.5 V vs. Ag/AgCl. Potential was applied for 1200 s before EIS measurements

It can be clearly seen that, at a content of 25 g NaF (Fig. 5c), the resistance of the passive layer of the titanium alloys is much lower. It shows this on reducing the corrosion resistance in this environment. Compared to the solution of artificial saliva without NaF, the resistance is 100 times greater (Fig. 5a), and for a content of 5 g NaF, it is 10 times higher (Fig. 5b).

Simulations of the EIS results obtained (Tab. 4) showed that the passive layer formed on the surface of both titanium alloys in the MAS solution with the addition of NaF is formed in two stages. The adapted electric equivalent circuit contains two time constants that are attributed to the existence of a passive layer and the build-up of corrosive products over the course of time (in this case, compounds with fluorine). In order to characterize the passive layer, a constant-phase CPE element was introduced into the circuit, which is characterized by two constants (T and P). Comparing the values obtained for CPE1-P (exponent P for CPE) in each of the used solutions value > 0.83, which indicates the capacitive properties of the passive layer of each alloy. Nevertheless, for the Ti-6Al-4V alloy, the CPE1-P values are lower than for the Ti-10Mo-4Zr alloy (above 0.9).

The obtained CPE2-P values for both titanium alloys differ more depending on the electrolyte used. For 5 g NaF in solution, CPE2-P takes values between 0.62–0.66, which suggests that there is an addition of ion diffusion (Fig. 6b) through the corrosion product layer (Fig. 5b). In the Bode plot, it is noteworthy that the frequency characteristics are of a similar shape at a wide range of frequencies. The difference in the value of the phase shift angle is visible for both alloys at high frequencies. A much higher phase angle occurs for the Ti-10Mo-4Zr alloy (approximately −81°). This means it has a higher corrosion resistance as compared to the Ti-6Al-4V alloy (for which the phase shift angle is around −71°).

For a solution containing 25 g NaF, the corrosion behavior of the passive layer is not the same for the titanium alloys (Fig. 5c). Mainly due to the use of an electric equivalent circuit comprising a resistance of R3 (Fig. 6a) the Ti-10Mo-4Zr alloy is composed of a double layer with better capacitive

properties (a CPE2-P close to 1) and a higher R3 value than R2 (~1300 $\Omega \cdot cm^2$). On the other hand, the Ti-6Al-4V alloy is characterized by a lower CPE2-P value, which may ambiguously indicate the structure of the passive layer: an intermediate state between the capacitive properties of the layer and the occurring diffusion processes. In each case, the resistance of the electrolyte (R1) and resistance of R2 decreases as the NaF content in the MAS increases.
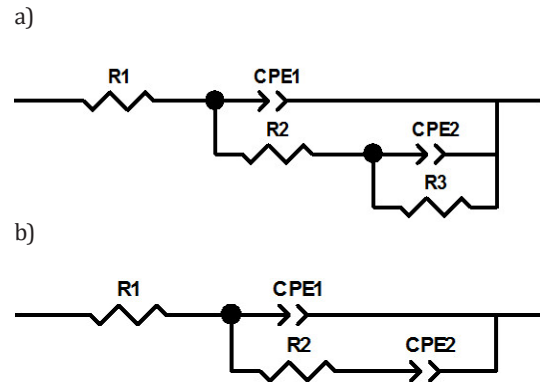

Fig. 6. Electric equivalent circuit from simulation for Ti-6Al-4V and Ti-10Mo-4Zr titanium alloys in MAS with (a) 5 g NaF and (b) 25 g NaF

4. CONCLUSIONS

The sodium fluoride concentration in a saliva solution has a significant influence on the electrochemical behavior of titanium alloys. Proportionally to the increase in the concentration of fluoride ions in the saliva solution, the corrosion resistance of titanium alloys decreases. At low concentrations of fluoride ions, the diffusion phenomena occur in the layer of corrosive products. The differences in the behavior of titanium alloys are noticeable at higher concentrations of fluoride ions, where the Ti-10Mo-4Zr alloy has a typical two-layer structure, having capacitive properties with a lower resistance in the outer layer. The Ti-6Al-4V alloy forms a layer that ambiguously corresponds to the capacitive layer as well as the phenomenon of diffusion through the corrosion products.

Table 4
Values of fitted parameters of equivalent circuit as function of applied potential 0.5 V vs. Ag/AgCl of Ti-6Al-4V and Ti-10Mo-4Zr alloys in MAS with different contents of NaF

Solution	Sample	R1, $\Omega \cdot cm^2$	R2, $\Omega \cdot cm^2$	CPE1-T $\times 10^{-5}$, $\Omega \cdot cm^{-2}s^{\varphi}$	CPE1-P	R3, $\Omega \cdot cm^2$	CPE2-T $\times 10^{-4}$, $\Omega \cdot cm^{-2}s^{\varphi}$	CPE2-P
MAS	Ti-6Al-4V	94.9	39,800	2.1	0.83	–	0.21	0.53
	Ti-10Mo-4Zr	77.4	23,900	2	0.9	334,400	0.19	0.75
MAS + 5 g NaF	Ti-6Al-4V	22.5	7833	4.3	0.86	–	11.6	0.66
	Ti-10Mo-4Zr	16.6	12,085	2.8	0.94	–	5.6	0.62
MAS + 25 g NaF	Ti-6Al-4V	5.9	1224	5.3	0.86	1011	12.1	0.79
	Ti-10Mo-4Zr	4.3	658.4	4.1	0.91	1280	9.8	0.98

Acknowledgements

REFERENCES

[1] Alves V.A., Reis R.Q., Santos I.C.B., Souza D.G., de F. Gonçalves T., Pereira-da-Silva M.A., Rossi A.& da Silva L.A. (2009). In situ impedance spectroscopy study of the electrochemical corrosion of Ti and Ti-6Al-4V in simulated body fluid at 25°C and 37°C. *Corrosion Science*, 51(10), 2473–2482. Doi:10.1016/j.corsci.2009.06.035.

[2] Kim E.-J., Jeong Y.-H., Choe H.-C. & Brantley W. (2012). Surface phenomena of HA/TiN coatings on the nanotubular-structured beta Ti-29Nb-5Zr alloy for biomaterials. *Applied Surface Science*, 258(6), 2083–2087. Doi:10.1016/j.apsusc.2011.04.051.

[3] Hsu R. W.-W., Yang C.-C., Huang C.-A. & Chen Y.-S. (2004). Investigation on the corrosion behavior of Ti-6Al-4V implant alloy by electrochemical techniques. *Materials Chemistry and Physics*, 86(2–3), 269–278. Doi:10.1016/j.matchemphys.2004.02.025.

[4] Sivakumar B., Kumar S. & Sankara Narayanan T.S. (2011). Fretting corrosion behaviour of Ti-6Al-4V alloy in artificial saliva containing varying concentrations of fluoride ions. *Wear*, 270(3–4), 317–324. Doi:10.1016/j.wear.2010.09.008.

[5] Biesiekierski A., Ping D.H., Yamabe-Mitarai Y. & Wen C. (2014). Impact of ruthenium on microstructure and corrosion behavior of β-type Ti-Nb-Ru alloys for biomedical applications. *Materials and Design*, 59, 303–309. Doi:10.1016/j.matdes.2014.02.058.

[6] Cui W.F., Jin L. & Zhou L. (2013). Surface characteristics and electrochemical corrosion behavior of a pre-anodized microarc oxidation coating on titanium alloy. *Materials Science and Engineering: C*, 33(7), 3775–3779. Doi:10.1016/j.msec.2013.05.011.

[7] Milošev I., Žerjav G., Calderon Moreno J.M. & Popa M. (2013). Electrochemical properties, chemical composition and thickness of passive film formed on novel Ti-20Nb-10Zr-5Ta alloy. *Electrochimica Acta*, 99, 176–189. Doi:10.1016/j.electacta.2013.03.086.

[8] Mohan L. & Anandan C. (2013). Wear and corrosion behavior of oxygen implanted biomedical titanium alloy Ti-13Nb-13Zr. *Applied Surface Science*, 282(1), 281–290. Doi:10.1016/j.apsusc.2013.05.120.

[9] Krawiec H., Vignal V., Loch J. & Erazmus-Vignal P. (2015). Influence of plastic deformation on the microstructure and corrosion behaviour of Ti-10Mo-4Zr and Ti-6Al-4V alloys in the Ringer's solution at 37°C. *Corrosion Science*, 96, 160–170. Doi:10.1016/j.corsci.2015.04.006.

[10] Tsutsumi Y., Niinomi M., Nakai M., Tsutsumi H., Doi H., Nomura N. & Hanawa T. (2012). Micro-arc oxidation treatment to improve the hard-tissue compatibility of Ti-29Nb-13Ta-4.6Zr alloy. *Applied Surface Science*, 262, 34–38. Doi:10.1016/j.apsusc.2012.01.024.

[11] Diomidis N., Mischler S., More N.S. & Roy M. (2012). Tribo-electrochemical characterization of metallic biomaterials for total joint replacement. *Acta Biomaterialia*, 8(2), 852–859. Doi:10.1016/j.actbio.2011.09.034.

[12] Zhao C., Zhang X. & Cao P. (2011). Mechanical and electrochemical characterization of Ti-12Mo-5Zr alloy for biomedical application. *Journal of Alloys and Compounds*, 509(32), 8235–8238. Doi:10.1016/j.jallcom.2011.05.090.

[13] Wang Z., Huang W. & Ma Y. (2014). Micro-scale abrasive wear behavior of medical implant material Ti-25Nb-3Mo-3Zr-2Sn alloy on various friction pairs. *Materials Science and Engineering C*, 42, 211–218. Doi:10.1016/j.msec.2014.05.039.

[14] González M., Peña J., Gil F.J. & Manero J.M. (2014). Low modulus Ti-Nb-Hf alloy for biomedical applications. *Materials Science and Engineering C*, 42, 691–695. Doi:10.1016/j.msec.2014.06.010.

[15] Diomidis N., Mischler S., More N.S., Roy M. & Paul S.N. (2011). Fretting-corrosion behavior of β titanium alloys in simulated synovial fluid. *Wear*, 271(7–8), 1093–1102.

[16] Castro M., Ponces M.J., Lopes J.D. & Pollmann M.C.F. (2015). Orthodontic wires and its corrosion – The specific case of stainless steel and beta-titanium. *Journal of Dental Sciences*, 10(1), 1–7. Doi:10.1016/j.jds.2014.07.002.

[17] Loch J., Krawiec H., Łukaszczyk A. & Augustyn-Pieniążek J. (2016). Corrosion resistance of titanium alloys in the artificial saliva solution. *Journal of Achievements in Materials and Manufacturing Engineering*, 74(1), 29–36.

[18] Sampaio M., Buciumeanu M., Henriques B., Silva F.S., Souza J.C.M. & Gomes J.R. (2015). Tribocorrosion behavior of veneering biomedical PEEK to Ti6Al4V structures. *Journal of the Mechanical Behavior of Biomedical Materials*, 54, 123–130. Doi:10.1016/j.jmbbm.2015.09.010.

[19] Mareci D., Chelariu R., Gordin D.M., Ungureanu G. & Gloriant T. (2009). Comparative corrosion study of Ti-Ta alloys for dental applications. *Acta Biomaterialia*, 5(9), 3625–3639. Doi:10.1016/j.actbio.2009.05.037.

[20] Schiff N., Grosgogeat B., Lissac M. & Dalard F. (2002). Influence of fluoride content and pH on the corrosion resistance of titanium and its alloys. *Biomaterials*, 23(9), 1995–2002. Retrieved from http://www.ncbi.nlm.nih.gov/pubmed/11996041 (accessed 25.06.2018).

[21] Souza J.C.M., Ponthiaux P., Henriques M., Oliveira R., Teughels W., Celis J.-P. & Rocha L. A. (2013). Corrosion behaviour of titanium in the presence of Streptococcus mutans. *Journal of dentistry*, 41(6), 528–34. Doi:10.1016/j.jdent.2013.03.008.

[22] PN-EN ISO 10993-15. (2005). Biologiczna ocena wyrobów medycznych – Cz. 15; Identyfikacja i oznaczanie ilościowe produktów degradacji metali i stopów.

[23] Vieira A.C., Ribeiro A.R., Rocha L. & Celis J.P. (2006). Influence of pH and corrosion inhibitors on the tribocorrosion of titanium in artificial saliva. *Wear*, 261(9), 994–1001. Doi:10.1016/j.wear.2006.03.031.

[24] Souza J.C.M., Barbosa S.L., Ariza E., Celis J.-P. & Rocha L. (2012). Simultaneous degradation by corrosion and wear of titanium in artificial saliva containing fluorides. *Wear*, 292–293, 82–88. Doi:10.1016/j.wear.2012.05.030.

[25] Huang H.-H. & Lee T.-H. (2005). Electrochemical impedance spectroscopy study of Ti-6Al-4V alloy in artificial saliva with fluoride and/or bovine albumin. *Dental Materials*, 21(8), 749–755. Doi:10.1016/j.dental.2005.01.009.

[26] Sakairi M., Kinjyo M. & Kikuchi T. (2011). Repassivation behavior of titanium in artificial saliva investigated with a photon rupture method. *Electrochimica Acta*, 56(4), 1786–1791. Doi:10.1016/j.electacta.2010.08.090.

[27] Loch J., Krawiec H. & Łukaszczyk A. (2015). Wpływ fluorków i kwasu mlekowego na odporność korozyjną stopów tytanu w symulowanym roztworze sztucznej śliny. *Archives of Foundry Engineering*, 1(4), 87–90.

[28] Takemoto S., Hattori M., Yoshinari M., Kawada E. & Oda Y. (2005). Corrosion behavior and surface characterization of titanium in solution containing fluoride and albumin. *Biomaterials*, 26(8), 829–837. Doi:10.1016/j.biomaterials.2004.03.025.

[29] Golvano I., Garcia I., Conde A., Tato W. & Aginagalde A. (2015). Influence of fluoride content and pH on corrosion and tribocorrosion behaviour of Ti13Nb13Zr alloy in oral environment. *Journal of the Mechanical Behavior of Biomedical Materials*, 49, 186–196. Doi:10.1016/j.jmbbm.2015.05.008.

[30] Dąbrowska E., Balunowska M. & Letko R. (2001). Zagrożenia wynikające z nadmiernej podaży fluoru. *Nowa Stomatologia*, 4, 22–27.

[31] Nakai H., Morita H., Tomasello P. & Nakatsuji H. (1998). Electronic structures of MoF6 and MoOF4 in the ground and excited states: A SAC-CI and frozen-orbital-analysis study. *Journal of Physical Chemistry A*, 102(11), 2033–2043. Doi:10.1021/jp973052s.

Novel Measurement Method to Study Thermal Aspects of Molding Mixture Decomposition

József Tamás Svidró[a]*, Attila Diószegi[a]

[a] Jönköping University School of Engineering, Department of Materials and Manufacturing, Gjuterigatan 5
Box 1026, SE-55111 Jönköping, Sweden
*e-mail: jozsef.svidro@ju.se

Abstract

A wide variety of molding mixtures are extensively used in the process of the sand casting of metal components today. The sector is continuously developing in production volume; moreover, the expectations of customers are increasing on a monthly basis (also from a quality point of view). Even though mold and core manufacturing are well-organized routines in most foundries, technological problems still appear that can lead to technological problems and casting defects. These trends are forcing metal casters to come up with fitting strategies to solve their daily production challenges, while their suppliers are expected to keep up the continuous development of their existing foundry products and to find innovative solutions as well as new material combinations. Research on molding materials and their properties must, therefore, take a step forward accordingly to generate the necessary new knowledge to understand the behavior of mold and core mixtures during casting.
This paper summarizes the latest results of a novel measurement method suitable for studying the degradation characteristics of different molding materials from a new perspective. The fundamentals of the method are based on a thermal analysis, focusing on the heat-absorption behavior of greensand and two types of chemically bonded sands regardless of the binder type and amount or the manufacturing process.

1. INTRODUCTION

Thermal analysis in the form of recording and interpreting temperature variations of a cooled or heated material over time is widely used today in foundry technology [1]. The broad areas of application mainly cover works based on cooling curve analyses of both non-ferrous and ferrous alloys [2–4]. Recently, studies applying traditional methods such as TG-DSC-DTG have been conducted to examine materials that are applicable as bonding agents in foundry purpose mold and core-making technologies [5]. Other sand-related works deal with the measurement of thermophysical properties in greensand molds while applying real foundry conditions [6, 7].

The proposed measurement method is based on Fourier thermal analysis (FTA) and is used in an inverse way to interpret the heat distribution versus time curves recorded in sand samples. The aim was to obtain a new understanding of the thermal aspects of the degradation processes in various molding mixtures. Thus, the heat absorption behavior by mixture decomposition was measured and calculated.

2. EXPERIMENTAL SETUP AND MATERIALS

The foundation of the experimental setup is the application of spherical sand samples of 40, 50, and 60 mm diameters.

Two N-type thermocouples with stainless steel sheaths were placed in the specimens with the aim to record the temperature; one in the geometrical center, and another at a lateral measuring point near the sample wall (Fig. 1).
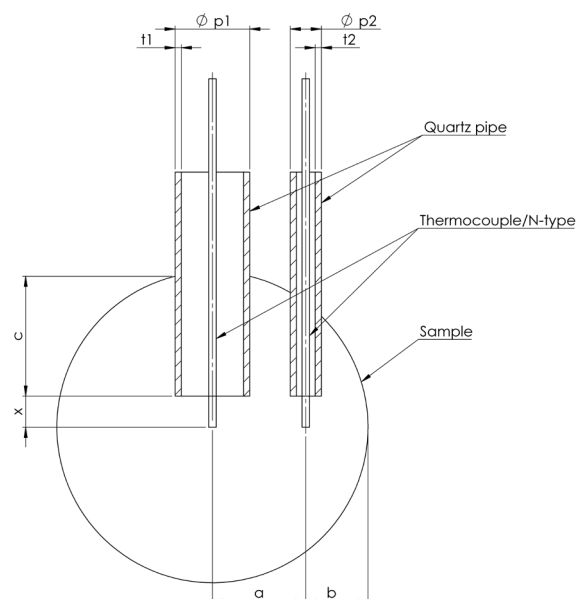

Fig. 1. Sample geometry [8–10]

Protective pipes of quartz glass with a wall thickness of 1 mm (*t*1 and *t*2 in Figure 1) were used to protect the thermocouples as the specimens are immersed into liquid metal during the measurement. The diameters of the protective pipes (ø*p*1 and ø*p*2 in Figure 1) were chosen according to previous works [8–10]. The size variations of the specimens and their direct contact with the liquid metal (as a heat source) during the tests ensured real foundry conditions. The exact locations of the temperature-reading points concerning all three diameters were according to Table 1.

Table 1
Positions of measuring points

Diameter of specimen, mm	Dimensions, mm			
	a	*b*	*c*	*x*
40	10	10	15	5
50	15	10	20	5
60	20	10	25	5

The molding mixtures investigated in this work were greensand, epoxy-SO_2, and polyurethane cold-box (PUCB) chemically bonded systems. They were all prepared with the same type of washed and screened silica sand with a light brown color, sub-rounded shape, and a medium grain size of 0.23 mm. The composition variables were set according to the typical industrial application of each mixture (Tab. 2). The specimens were not coated before the measurements. The epoxy-SO_2 and PUCB mixtures were tested without drying; however, the greensand samples were dried for 2 hours at 105°C to increase their integrity for the thermocouple placement procedure. The samples were then immersed into liquid iron at 1300±10°C, and the temperature distribution in both measuring points was recorded.

Table 2
Production parameters of studied mixtures

Mixture	Composition, wt.%*
Greensand	8% bentonite, 3.3% water, 3% coal dust
Epoxy-SO_2	1% epoxy resin + 30%** hydroperoxide (cured by SO_2 gas)
PUCB	0.9% phenolic resin + 0.9% isocyanate (cured by amine vapor)

* by mass of sand
** by mass of resin

3. RESULTS AND DISCUSSION

In this paper, the results of the 50-mm-diameter samples were primarily considered for further investigations. Figure 2 shows the temperature distribution over time in the 50-mm-diameter samples of all three mixtures. The temperature recordings at the lateral points near the sample walls showed faster heating (Fig. 2b) when compared to the curves at the central measuring point (Fig. 2a). The differences in the heating rates were due to the various distances of the temperature-recording positions from the heat source.
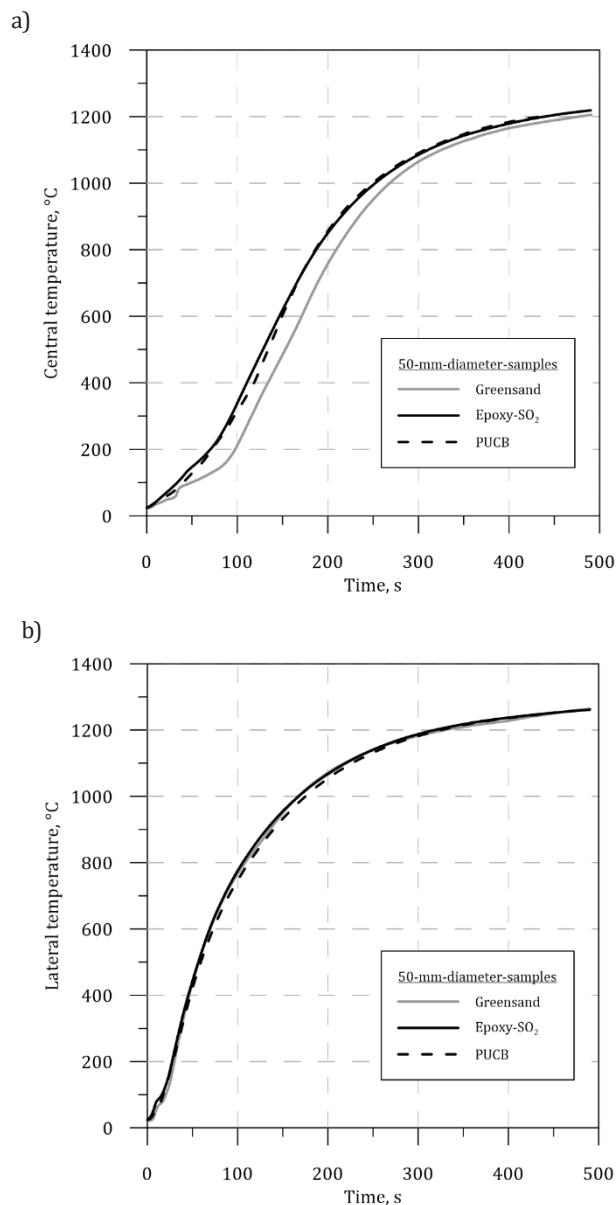

Fig. 2. Temperature distribution versus time in centers of 50-mm-diameter samples (a) and near sample walls (b) for all studied mixtures

On the other hand, differences due to the various binder types in the mixtures did not clearly appear. The reason for this is that the temperature of the liquid iron ensured a generally high heating rate and the relatively fast procession of the expected heat absorbing and binder degradation processes. Therefore, with the aim to learn more about the differences between the three mixtures, the heating curves were further processed by Fourier thermal analysis. Based on the initial measurements of the temperature distribution inside the samples, a Fourier

thermal analysis was run, and the total absorbed heat values (*L*) were calculated for the 50-mm-diameter specimens of each mixture (shown in the legends of Figures 3–5). These values correspond to the amount of heat taken away from the melt by different processes; the decomposition of the bound and crystalline water in the lattice structure of the bentonite, the swelling and volatilization of the coal dust in the greensand, and the degradation of the organic resins and their catalysts and reactants in the chemically bonded mixtures. The results showed that greensand absorbed a significantly higher amount of heat as compared to the lower values of the epoxy-SO_2 and PUCB mixtures. The heat absorption behavior was further investigated by determining its temperature dependency by plotting the rate of heat absorption versus the temperature inside the geometrical centers of the samples (Figs. 3–5).

The heat absorption and degradation profile of the greensand and its features are shown in Figure 3. Heat absorption started intensively in the beginning, peaking at around 150°C in the sand; therefore, the vaporization process of the bound water took a significant amount of heat from the melt. At higher sand temperatures, the swelling and volatilization of the coal dust in the green sand produced additional maximum heat absorption peaks from between 300 and 550°C; however, this process overlapped the loss of crystalline water in the lattice structure of the bentonite. According to Figure 3, the heat absorption processes were finished in the greensand by up to 700°C.
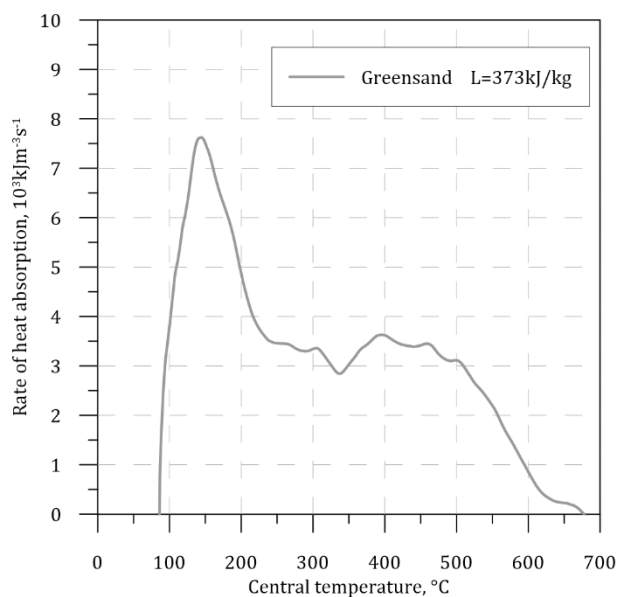

Fig. 3. Heat absorption and degradation profile of greensand versus temperature in center of 50-mm-diameter sample

Figure 4 shows the heat absorption and degradation profile of the epoxy-SO_2 mixture. The heat absorption reached an initial maximum at lower sand temperatures (150°C) due to the vaporization of the free moisture and bound water in the system (but at a significantly lower rate when compared to the greensand result). The endothermic process of the epoxy resin degradation started as the temperature rose in the sample and continued until 500°C. This process

was assumed to overlap the combustion of the degradation products. Besides the initial peak, the epoxy-SO_2 mixture showed a relatively smooth heat absorption and degradation profile.
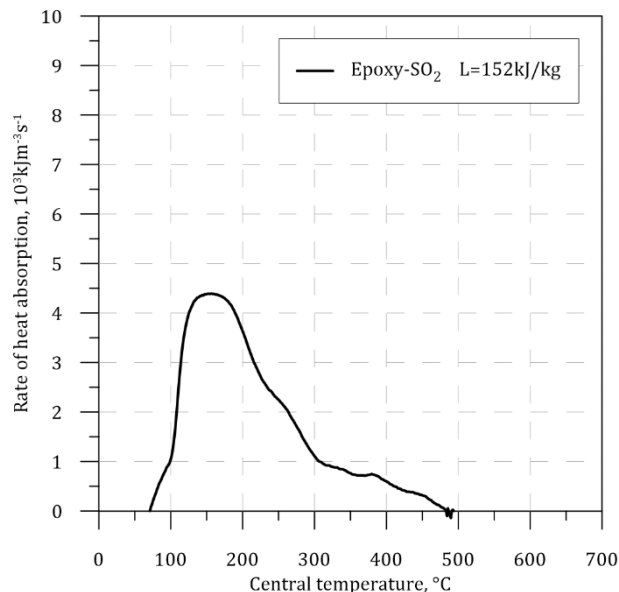

Fig. 4. Heat absorption and degradation profile of epoxy-SO_2 mixture versus temperature in center of 50-mm-diameter sample

The heat absorption and degradation characteristic of the PUCB mixture are shown in Figure 5. The rate of heat absorption reached the initial maximum shortly above 100°C (similar to the epoxy-SO_2 system) when the decomposition of the free moisture and bound water in the mixture components occurred. However, the degradation of the polyurethane showed multiple major stages at 250°C and 350–450°C as notable maximums of heat absorption appeared on the curves. The PUCB mixture, therefore, displayed a more complex multi-staged decomposition process.
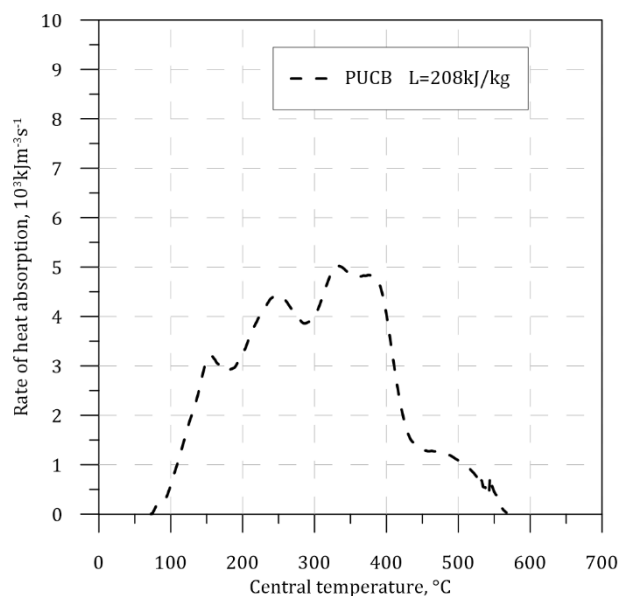

Fig. 5. Heat absorption and degradation profile of PUCB mixture versus temperature in center of 50-mm-diameter sample

4. CONCLUSION

In this work, conventional molding mixtures were studied by a new method based on Fourier thermal analysis. The results showed that greensand absorbed considerably more heat from the liquid metal than chemically bonded systems such as epoxy-SO_2 and PUCB mixtures. All three mixtures showed diverse degradation profiles. The heat absorption behavior can be directly interpreted as the cooling ability of the mixtures.

Greensand exhibited a major maximum peak of heat absorption and cooling ability at lower sand temperatures, together with additional maximums due to the swelling and volatilization of the coal dust at higher sand temperatures. The studied chemically bonded mixtures also showed initial maximums but at a moderate rate when compared to the greensand as well as similar multiple peaks at the later stages of the degradation by the PUCB mixture. The epoxy-SO_2 mixture showed a relatively smooth heat absorption and degradation profile.

The maximums of the heat absorption at specific sand temperatures is expected to eventuate in the improved cooling ability of the cores, which is expected to shorten the solidification time in the casting (affecting its final microstructural morphology) and may result in large variations in the mechanical properties. Future work is, therefore, planned to further study and prove the relationship between the heat absorption capacity of sand mixtures and the mechanical properties of castings.

Acknowledgements

REFERENCES

[1]   Stefanescu D.M. (2015). Thermal Analysis – Theory and applications in metal casting. *International Journal of Metalcasting*, 9(1), 7–22. Doi:10.1007/BF03355598.

[2]   Krupiński M., Krupińska B., Rdzawski Z., Labisz K. & Tański T. (2015). Additives and thermal treatment influence on nonferrous alloys. *Journal of Thermal Analysis and Calorimetry*, 120(3), 1573–1583. Doi:10.1007/s10973-015-4497-0.

[3]   Bartosová M., Pribulová A., Eperjesi S. & Futás P. (2018). Analyisis of cooling curves of nodular cast iron. *Journal of Casting and Materials Engineering*, 2(1), 1–4. Doi:10.7494/jcme.2018.2.1.1.

[4]   Diószegi A., Diaconu V.L. & Fourlakidis V. (2016). Prediction of volume fraction of primary austenite at solidification of lamellar graphite cast iron using thermal analyses. *Journal of Thermal Analysis and Calorimetry*, 124(1), 215–225. Doi:10.1007/s10973-018-7088-z.

[5]   Grabowska B., Malinowski P., Szucki M. & Byczyński L. (2016). Thermal analysis in foundry technology. *Journal of Thermal Analysis and Calorimetry*, 126(1), 245–250. Doi:10.1007/s10973-016-5435-5.

[6]   Krajewski P.K. & Piwowarski G. (2015). Range of thermal conductivity changes of wet green foundry sand during casting solidification. *Archives of Metallurgy and Materials,* 60(3B), 2391–2395.

[7]   Krajewski P.K., Piwowarski G., Żak P.L. & Krajewski W.K. (2014). Experiment and numerical modelling the time of plate-shape casting solidification vs. thermal conductivity of mould material. *Archives of Metallurgy and Materials*, 59(4), 1405–1408. Doi:10.1515/amm-2015-0390.

[8]   Lidumnieks K., Svidró J.T. & Diószegi A. (2017). The effect of various production parameters on the heat absorbing capacity of greensand. *International Journal of Cast Metals Research*, 31(1), 7–13. Doi:10.1080/13640461.2017.1348005.

[9]   Svidró J.T., Diószegi A., Svidró J. & Ferenczi T. (2017). Thermophysical aspects of reclaimed sand addition to the epoxy-SO_2 coremaking system studied by Fourier thermal analysis. *Journal of Thermal Analysis and Calorimetry*, 130(3), 1779–1789. Doi:10.1007/s10973-017-6612-x.

[10] Svidró J.T., Diószegi A., Svidró J. & Ferenczi T. (2017). The effect of different binder levels on the heat absorption capacity of moulding mixtures made by the phenolic urethane cold-box process. *Journal of Thermal Analysis and Calorimetry,* 130(3), 1769–1777. Doi:10.1007/s10973-017-6611-y.